




Electrochromic properties of hydrothermally grown microstructured V₂O₅ and MWCNT/V₂O₅ composite films

Mudaliar Mahesh Margoni^{1,2,*} , S. Mathuri³, K. Ramamurthi¹, V. Ganesh¹, R. Ramesh Babu⁴, and K. Sethuraman⁵

¹Crystal Growth and Thin Film Laboratory, Department of Physics and Nanotechnology, Faculty of Engineering and Technology, SRM Institute of Science and Technology, Kancheepuram District, Kattankulathur, Tamil Nadu 603 203, India

²Present address: Department of Mechanical Engineering, Faculty of Mathematical and Physical Sciences, University of Chile, Santiago, Chile

³Institute for Advanced Study and Institute of Microscale Optoelectronics, Shenzhen University, Shenzhen, China

⁴Crystal Growth and Thin Film Laboratory, Department of Physics, Bharathidasan University, Tiruchirappalli, Tamil Nadu 620024, India

⁵Department of Material Science, School of Technology, Central University of Tamil Nadu, Thiruvavur, Tamil Nadu 610 005, India

Received: 18 July 2022

Accepted: 20 September 2022

Published online:

1 October 2022

© The Author(s), under exclusive licence to Springer Science+Business Media, LLC, part of Springer Nature 2022

ABSTRACT

Vanadium pentoxide (V₂O₅) and multiwalled carbon nanotubes added V₂O₅ composite (MWCNT/V₂O₅) films were prepared by hydrothermal technique. The influence of various levels of MWCNT on the electrochromic properties of MWCNT/V₂O₅ films was investigated. X-ray diffraction analysis revealed that the films are polycrystalline in nature and belong to orthorhombic crystal system of V₂O₅. Raman and FTIR spectral analyses confirmed the formation of V₂O₅ phase and the influence of MWCNT on the vibrational frequencies of V₂O₅ films. V₂O₅ film added with 1 wt.% MWCNT showed enhanced transmittance and the bandgap of V₂O₅ increases with further increase in the addition of MWCNT in V₂O₅ films. The electrochromic studies revealed electrochromic reversibility of 82% (1 wt.% MWCNT added film) and 82.5% (5 wt.% MWCNT added film) whereas after 100 cycles the films added with 1 wt.% and 5 wt.% of MWCNT acquired excellent electrochromic reversibility of 92% and 88%, respectively. Further the switching kinetics of the film added with 1 wt.% MWCNT is 1.8 s for coloration and 2.4 s for bleaching processes.

Address correspondence to E-mail: maheshmdlr@gmail.com

1 Introduction

Electrochromic materials find wide range of applications in the large area display, energy efficient glazing and smart windows [1]. Transition metal oxides exhibit color changes and high coloration efficiency because of their electrochromic characteristics that arise from the reversible redox reaction of the transition metal ions. This reaction process involves electron–ion intercalation/deintercalation due to the applied potential [2]. Among the transition metal oxides such as tungsten oxide (WO_3), titanium dioxide (TiO_2), vanadium pentoxide (V_2O_5), nickel oxide (NiO) and iridium oxide (IrO_2), vanadium pentoxide has attracted great attention in the area of electrochromic applications because of its multiple oxidation states (V^{2+} to V^{5+}), multi electrochromic behavior and high reversibility [3]. Various deposition techniques such as spray pyrolysis [4], spin coating [5], hydrothermal [6], sputtering [7] and doctor blade [8] methods were employed to deposit V_2O_5 films. However, V_2O_5 has its limitation to use it in electrochromic devices and lithium ion (Li^+) batteries due to its low electronic conductivity, slow ion diffusion rate and poor cycling stability [9, 10].

The literature survey reveals that various researchers have proposed different approaches for enhancing the electrical conductivity, structural stability, Li^+ ions intercalation and deintercalation properties and the electrochemical properties of V_2O_5 . The effect of adding various transition metal ions and carbonaceous materials such as single walled carbon nanotubes (SWCNT), multi walled carbon nanotubes (MWCNT) and graphene possessing unique structure, superior electronic, optical and mechanical properties to modify the properties of V_2O_5 was investigated [11, 12]. Metallic dopants introduced in V_2O_5 matrix replace the vanadium atoms and enhance the electrical properties. In general, the metal dopant atom forming an octahedral chain makes the material structure more stable during electrochemical cycling and improves the system's reversibility [13]. Wei et al. [14] reported that Ti doping with the V_2O_5 film makes the films amorphous and gives more space for Li^+ ions to intercalate and deintercalate which increases the transmittance and improves cyclic switching stability. Panagopoulou et al. [13] reported that 15 at.% Mg doped V_2O_5 films improved coloration efficiency to $44.5 \text{ cm}^2 \text{ C}^{-1}$ at 750 nm and to $71.3 \text{ cm}^2 \text{ C}^{-1}$ at

520 nm. Li et al. [15] reported that 3D porous structured V_2O_5 and $\text{Fe}_{0.1}\text{V}_2\text{O}_{5.15}$ thin films deposited by electrostatic spray deposition technique improved the stability and cycling performance of V_2O_5 due to incorporation of Fe^{3+} into V_2O_5 matrix. Zhang et al. [16] reported that V_2O_5 /graphene nanocomposite films prepared by dip-coating technique show multi color electrochromism and improved cycling stability and response time with enhanced optical modulatory range (from 20.6 to 30.8%). Zhi et al. [17] reported that V_2O_5 /reduced graphene oxide ($\text{V}_2\text{O}_5/\text{rGO}$) nanocomposite films deposited by a combined process of sol–gel and spin–coating method exhibit better cycling stability, faster switching speed, improved optical modulatory range and high coloration efficiency. Generally, CNTs show unique one-dimensional tubular structure, large surface area, high electrical conductivity and electrochemical stability which make them suitable candidates for energy storage and energy conversion applications [18]. Further, the combination of CNTs and V_2O_5 shows enhanced electrochemical performances with high discharge rates [19]. Thus the nanocomposites provide favorable diffusion pathways for both the electrons and lithium ions, which are essential in high rate rechargeable lithium-ion batteries and electrochromic devices [19].

The advantage of indulging hydrothermal technique for depositing inorganic material films involves the crystal growth process under the supercritical state of water and also the periodic change in physical and chemical properties of these materials [20]. Thus by altering the growth parameters of hydrothermal technique one can achieve the formation of single phase materials and control effectively their surface morphology and crystalline nature to tune the properties for required applications.

Comprehensive approaches towards modifying the V_2O_5 morphology by the addition of MWCNT employing hydrothermal technique are proved to be effective in making V_2O_5 for electrochemical applications. This composite structure of V_2O_5 can improve the electronic conductivity, the lithium-ion diffusion and cyclic stability. Furthermore, the resulting microstructured V_2O_5 morphology containing nanorods can be expected to increase the active areas for Li^+ diffusion in the composites; thus leading to fast response time for bleaching and coloring, better structural stability and cyclic stability. In the present study, we report a simple and unique

approach to grow V_2O_5 and MWCNT/ V_2O_5 composites via the hydrothermal technique for different concentrations of MWCNT (0, 1, 3 and 5 wt%). Further, we demonstrate that these MWCNT/ V_2O_5 composites have the ability to overcome the limitations of V_2O_5 and achieving improved electrochemical performance as cathode materials for electrochromic device applications.

2 Experimental section

2.1 Preparation of V_2O_5 and V_2O_5 /MWCNT composite films by hydrothermal method

The V_2O_5 and V_2O_5 /MWCNT composite films were prepared by hydrothermal method onto the fluorine doped tin oxide (FTO) glass substrates. V_2O_5 powder (0.2 g) was taken in a beaker containing 50 ml of double distilled water and stirred well. The process was performed in an oil bath at 80 °C. Then 1.97 g of oxalic acid was added to the above solution and stirred for 1 h to obtain VOC_2O_4 solution [21]. This solution was added with 500 ml double distilled water taken in a beaker. Then NH_4OH was added slowly to this VOC_2O_4 solution to adjust the solution pH \sim 2. This forms the aqua precursor solution. Precursor solution of 40 ml was utilized from 550 ml stock solution to deposit V_2O_5 films. To coat the V_2O_5 /MWCNT composite films, MWCNT of 1, 3 and 5 wt.% was added in separate experiments with 40 ml of the aqua precursor stock solution and was ultra-sonicated for 30 min. The FTO glass substrate of 1 cm \times 1 cm size was placed into the solution taken in a Teflon lined autoclave. The substrate was supported with a glass microslide such that the conducting side faces upwards and inclined at about 45° angle to the wall of Teflon. The hydrothermal temperature was fixed at \sim 230 °C and the duration of reaction was 4 h. Then the autoclave was naturally cooled to room temperature. The films obtained were greenish in color which indicates the formation of VO_2 phase [21]. Further these films were air annealed at 500 °C for 1 h to obtain the V_2O_5 films. The V_2O_5 /MWCNT films deposited from 0 wt.%, 1 wt.%, 3 wt.% and 5 wt.% MWCNT added precursor solutions are respectively named as films VC_0 , VC_1 , VC_3 and VC_5 .

2.2 Characterization studies

An X-ray diffractometer (X'pert PRO Panalytical powder X-ray diffraction system) was used to scan the samples with CuK_{α} radiation ($\lambda = 1.5405 \text{ \AA}$) in Bragg–Brentano geometry ($\theta/2\theta$ coupled) in the 2θ range (20°–90°) to study the structural properties. Field emission scanning electron microscopy (FEI Quanta FEG200) was used to study the surface morphology. UV–Vis–NIR spectrophotometer (Specord-200) was employed to measure the transmittance of the films in the 300–1100 nm wavelength range. The room temperature electrical studies were carried out employing Ecopia HMS-3000 with a magnetic field of 0.57 T (van der Pauw configuration). The electrochromic cell consists of a conventional three electrodes, in which the V_2O_5 /MWCNT composite films deposited onto FTO glass substrates, platinum and Ag/AgCl respectively served as working electrode, counter electrode and the reference electrode. Lithium perchlorate ($LiClO_4$) (1 M) in propylene carbonate (100 ml) was employed as the electrolyte solution. The cyclic voltammetry (CV), chronoamperometry (CA), chronocoulometry (CC) and impedance measurements were carried out using CHI604E electrochemical workstation.

3 Results and discussion

3.1 X-ray diffraction analysis

The X-ray diffraction (XRD) pattern of V_2O_5 film (VC_0) and V_2O_5 /MWCNT composites (VC_1 – VC_5) deposited onto FTO glass substrates by hydrothermal technique along with that of the bare FTO glass substrate are presented in Fig. 1a. XRD pattern of polycrystalline V_2O_5 film and V_2O_5 /MWCNT composite films exhibit orthorhombic crystal system of V_2O_5 . All the films show XRD peaks at $2\theta \sim 15.3^\circ$, 17.6° , 20.2° and 21.5° due to respectively (200), (002), (001) and (101) planes that match well with the standard data (JCPDS card no. 41-1426). The XRD pattern of MWCNT powder, presented in Fig. 1b, match well with the reported XRD pattern [22]. Figure 1a shows that the peak intensity of (001) plane is reduced by adding 1, 3 and 5 wt.% of MWCNT. This is due to the influence of addition of MWCNT on the crystallinity of the deposited films. With the addition of 3 wt.% of MWCNT the growth of the film along

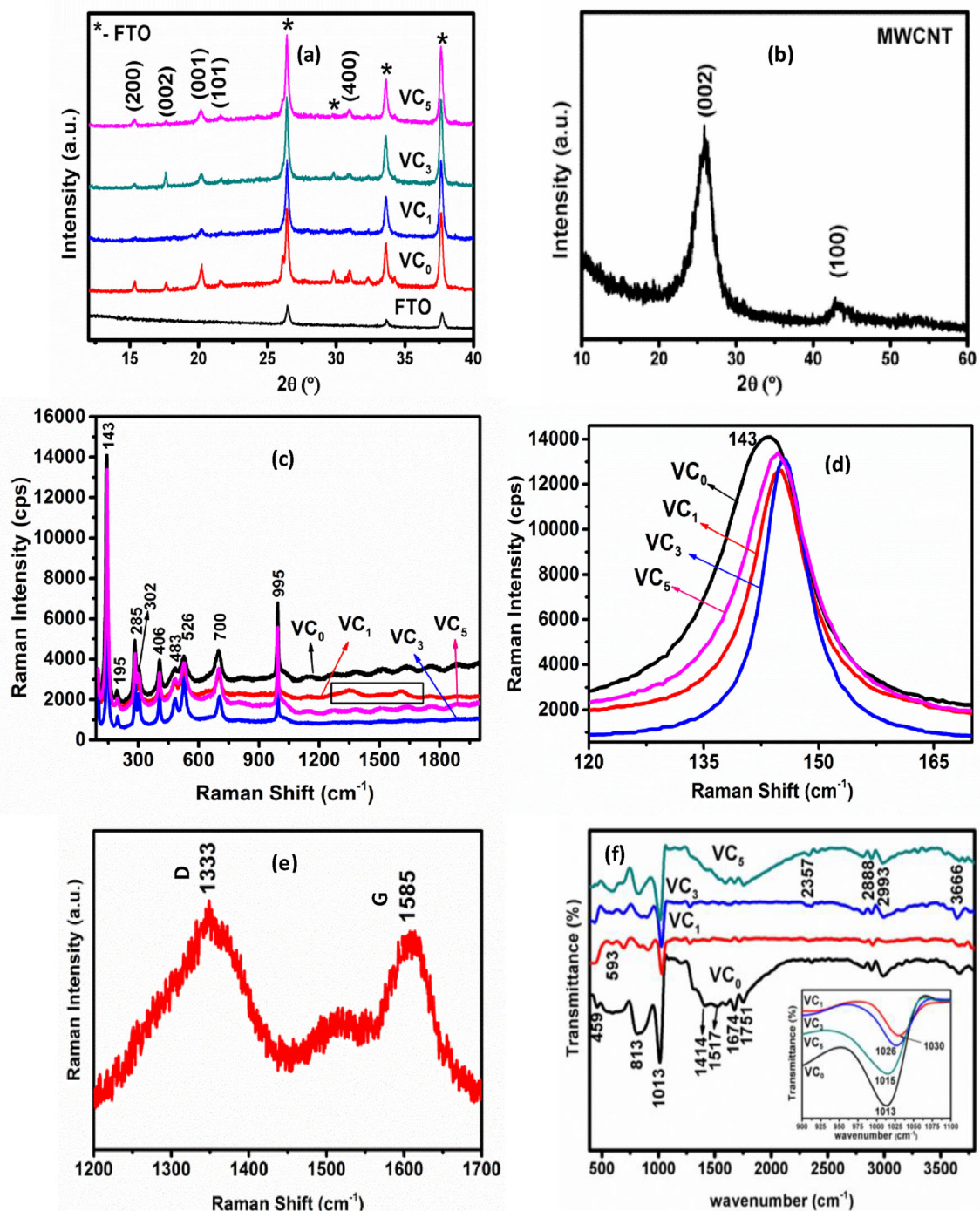


Fig. 1 **a** XRD pattern of the films VC₀, VC₁, VC₃ and VC₅ and FTO glass substrate; **b** XRD pattern of MWCNT powder; **c** Raman spectra of the films VC₀, VC₁, VC₃ and VC₅; **d** Zoomed peak at ~ 143 cm⁻¹ shows Raman shift; **e** D and G

Raman band peaks of MWCNT observed for the film VC₁; and **f** FTIR spectra of the films VC₀, VC₁, VC₃ and VC₅ and the inset represents the shift in the peak at 1000 cm⁻¹ (Color figure online)

(001) is reduced and favored the growth along (002) plane. Addition of 5 wt.% of MWCNT reveals the saturated chemical interaction between the MWCNT and V₂O₅. This results in the growth of film along

(001) and the peak intensity is relatively increased when compared to 1 and 3 wt.% MWCNT/V₂O₅ composite films which show similar behavior as that

of V₂O₅ film. The crystallite size (*D*) was estimated using Scherrer equation [23],

$$D = \frac{K\lambda}{\beta \cos\theta},$$

where λ (1.5406 Å) is the X-ray wavelength; β is the full width at half maximum (FWHM) and θ is the Bragg diffraction angle, $K = 0.9$ is the so-called Scherrer constant. K depends on the crystallite shape and the size distribution indices the diffraction line [24]. The crystallite size (*D*) of the films VC₀, VC₁, VC₃ and VC₅ obtained from (002) plane are 24.0 nm, 21.0 nm, 14.0 nm and 21.0 nm, respectively. The crystallinity decreases with the addition of MWCNT in the matrix of V₂O₅.

Raman spectra of the films VC₀, VC₁, VC₃ and VC₅ are shown in Fig. 1c. The peaks observed at 143, 195, 285, 302, 406, 483, 526, 700 and 995 cm⁻¹ confirm the formation of V₂O₅ [25, 26]. The Raman frequencies of the present work are compared with the reported values in Table 1. The peak at 995 cm⁻¹ corresponds to V⁵⁺=O. The peak positioned at 700 cm⁻¹ is due to stretching mode of $\nu(V-O-V)$ s (doubly coordinated oxygen) which results from corner-shared oxygen common to two pyramids [27]. The peak at 526 cm⁻¹ is due to the stretching mode of $\nu(V-O)$ s (triply coordinated oxygen) which results from the edge shared oxygen atoms that is common to three pyramids. Peak at 483 cm⁻¹ is attributed to the bending vibration of the doubly coordinated oxygen bridging

(V–O–V) and the peak at 298 cm⁻¹ corresponds to triply coordinated oxygen (V–O) bond. The peaks at 406 and 285 cm⁻¹ are representing the bending vibration of the V=O bonds. The prominent peak at 143 cm⁻¹ and a weak peak at 195 cm⁻¹ are attributed to the lattice vibrations of V₂O₅ [25, 26].

Raman frequencies obtained for the films VC₀, VC₁, VC₃ and VC₅ match well with the earlier reports of V₂O₅ [25, 26]. The influence of addition of MWCNT in V₂O₅ matrix is seen in the peak shifts and decrement in the Raman peak intensities as shown in Fig. 1c. The peak shift observed at 143 cm⁻¹ (Fig. 1d) represents the disturbance in the layered structures of V₂O₅ due to the addition of MWCNT. The Raman peak of film VC₅ shows shift towards lower values when compared to film VC₁ and VC₃ which indicates the saturated chemical interaction between V₂O₅ and MWCNT. The Raman frequencies given in Table 1 show that the incorporation of MWCNT (1, 3 and 5 wt.%) in V₂O₅ does not effectively influence the magnitude of vibrational frequencies of V₂O₅. The V₂O₅/MWCNT composite film (film VC₁) shows two characteristics peaks of carbon at 1333 and 1585 cm⁻¹ [28] (also marked in Fig. 1e) as D and G bands for sp³ carbons (defect regions) and sp² carbons (graphitic regions) respectively [28]. The intensity of the peak at 995 cm⁻¹ of the films varies and no appreciable shift in the frequency is observed (Fig. 1c).

The Fourier transform infrared (FTIR) spectra recorded in the range 500–3800 cm⁻¹ for the V₂O₅

Table 1 Raman vibrational frequencies of the films VC₀, VC₁, VC₃ and VC₅ with the frequency assignment

Sr.no.	Assignment [25]	Raman peak (cm ⁻¹)					
		Present work				Previous work [Ref.]	
		VC ₀	VC ₁	VC ₃	VC ₅	[23]	[24]
1	Relative motions of V ₂ O ₅ layers with respect to each other	143	145	145	144	149	143
2	Relative motions of V ₂ O ₅ layers with respect to each other	195	196	196	195	201	197
3	$\delta(V=O)_b$	285	285	285	285	285	285
4	$\nu(V-O)_b$ Triply coordinated oxygen	298	301	301	301	306	303
5	$\delta(V=O)_b$	406	406	406	406	405	405
6	$\delta(V-O-V)_b$	483	483	483	483	482	481
7	$\nu(V3-O)_s$ Triply coordinated oxygen	526	526	526	526	533	525
8	$\nu(V-O-V)_s$ Doubly coordinated oxygen	700	700	700	700	698	701
9	$\nu(V=O)_s$	995	995	995	995	993	995

film and V_2O_5 /MWCNT composite films are displayed in Fig. 1f. Vibrational mode of vanadyl group observed in the FTIR spectra of the films, given in the inset of Fig. 1f, show a slight variation in the values. The bands observed at 1013, 810 and 590 cm^{-1} are assigned to the V=O stretching, V–O–V bending and V–O stretching modes, respectively [29]. The band at 1414 cm^{-1} belongs to bending mode of C–H [30] and the bands appearing at 1570 cm^{-1} and 1654 cm^{-1} correspond to OH vibrations [29, 31]. The bands observed at 2888 and 2993 cm^{-1} are attributed to symmetry and asymmetry stretching modes of CH_2 respectively which may be originated from the residual organics in the products or from MWCNTs [26]. The peak at 3666 cm^{-1} belongs to the stretching mode of OH [31]. The interaction between the V_2O_5 and MWCNTs increases the peak intensity for addition of 1 wt.% MWCNT whereas the peak intensity decreases with further increase in the MWCNT concentration. However 5 wt.% of MWCNT in V_2O_5 (VC_5) shows the peak intensity is nearly equal to that of VC_0 film, thus indicating the saturated chemical interactions between V_2O_5 and MWCNTs [32]. Thus, Raman and FTIR spectral studies coupled with XRD results confirm strong influence of 1 wt.% MWCNT on V_2O_5 films. Whereas 5 wt.% MWCNT added film (VC_5) shows saturated chemical interactions and hence exhibits similar properties as that of film VC_0 .

3.2 Surface morphology

The SEM images showing the surface morphology of the films VC_0 , VC_1 , VC_3 and VC_5 are given in Fig. 2. The magnified SEM images of the selected part of film VC_0 , VC_1 , VC_3 and VC_5 are shown in Fig. 2a₂–d₂—($1\text{ }\mu\text{m} \times 1\text{ }\mu\text{m}$) respectively. The surface of the V_2O_5 film (film VC_0) reveals the formation of hollow microspheres structures containing nanorods (Fig. 2a₁, a₂). The surface morphology of the film VC_1 reveals that 1 wt.% MWCNT in V_2O_5 yields relatively less number of microspheres formed by nanorods on the surface. This may be due to the influence of MWCNTs on the V_2O_5 nucleations (Fig. 2b₁, b₂). When the concentration of MWCNT is increased to 3 wt.% (Fig. 2c₁, c₂), the surface morphology of the film VC_3 shows formation of intense nanorods and less number of microspheres containing nanorods. The MWCNT (5 wt.%) in the film VC_5 modified the shape of morphology structures into microplates (Fig. 2d₁, d₂) as nearly those shapes formed on the film VC_0 .

The SEM images of the film VC_1 (Fig. 2e) and film VC_3 (Fig. 2f) (200 nm magnification) evidently exhibit the formation of nanorods, with varying size and density, below the hollow microspheres owing to the addition of MWCNT. Thus the size, shape and morphology of the nanorods and the microspheres of V_2O_5 formed by nanorods on the films are effectively modified by the various levels of MWCNT concentration added in the precursor solution.

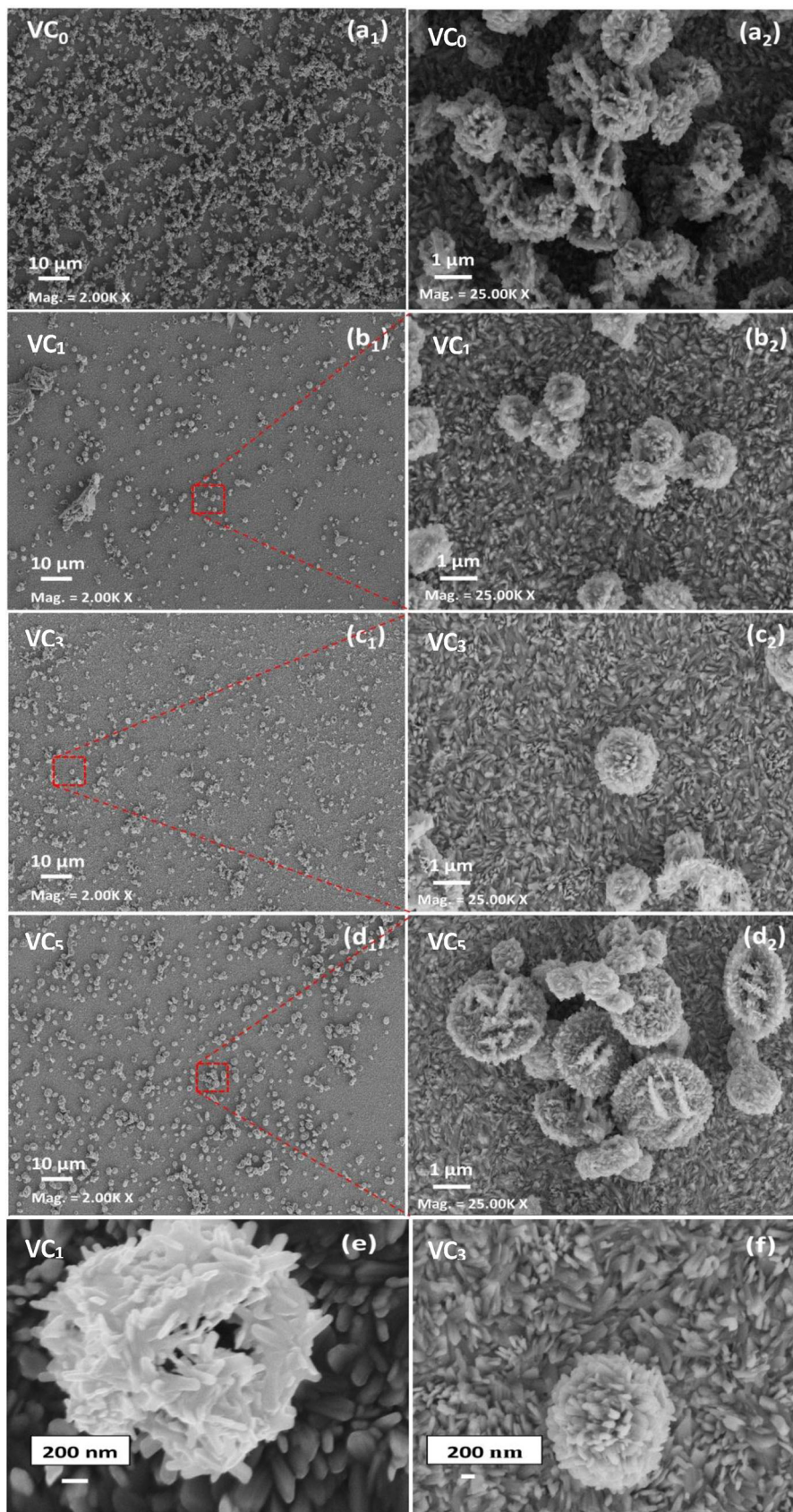
3.3 Optical analysis

The optical transmittance spectra of V_2O_5 films and V_2O_5 /MWCNT composite films recorded in the 350–1100 nm wavelength range are displayed in Fig. 3a. Table 2 presents the average visible transmittance (AVT) value obtained in the region (500–800 nm) and the wavelength at which maximum transmittance ($T_{\text{max.}\%}$) occurred for the films VC_0 , VC_1 , VC_3 and VC_5 . The AVT and $T_{\text{max.}\%}$ acquired by the film VC_1 is relatively high when compared to that of the other films due to formation of the hollow microspheres structures consisting nanorods (Fig. 2e). The shift in the absorption edge may be due to surface modification with varying MWCNT content in the films. The direct bandgap (E_g) of the coated films VC_0 , VC_1 , VC_3 and VC_5 was evaluated using Tauc plot relation [33]. The E_g values vary between 2.34 and 2.49 eV (Fig. 3b). The widening of E_g in films VC_1 , VC_3 and VC_5 is due to Burstein–Moss effect. The film VC_1 shows increase in the carrier concentration (Table 2) when compare with that of the other films which in turn increases the E_g [34, 35]. Thus the film VC_1 exhibits relatively higher $T_{\text{max.}\%}$ due to formation of hollow microspheres containing nanorod structures with respect to other films.

3.4 Electrical transport properties

The Hall measurement setup was employed to study the electrical transport properties of the films. Carrier concentration, mobility and resistivity of the coated films are presented in Table 2. The film VC_1 (addition of 1 wt.% MWCNTs in the precursor solution) shows increment in the carrier concentration. The slight increment in the mobility and conductivity observed in the films VC_1 , VC_3 and VC_5 when compare with that of film VC_0 is due to influence of MWCNT in V_2O_5 . The addition of 1 wt.% of MWCNT in V_2O_5

Fig. 2 Surface morphology of the films VC₀, VC₁, VC₃ and VC₅ with 10 μm × 10 μm magnification are presented in (a₁), (b₁), (c₁) and (d₁) respectively. Whereas the magnified surface morphology of the selected part of the film VC₀, VC₁, VC₃ and VC₅ are shown in (a₂), (b₂), (c₂) and (d₂) with 1 μm × 1 μm magnification respectively. In this figure (e) and (f) represents the SEM images of the film VC₁ and film VC₃ respectively with 200 nm × 200 nm magnification (Color figure online)



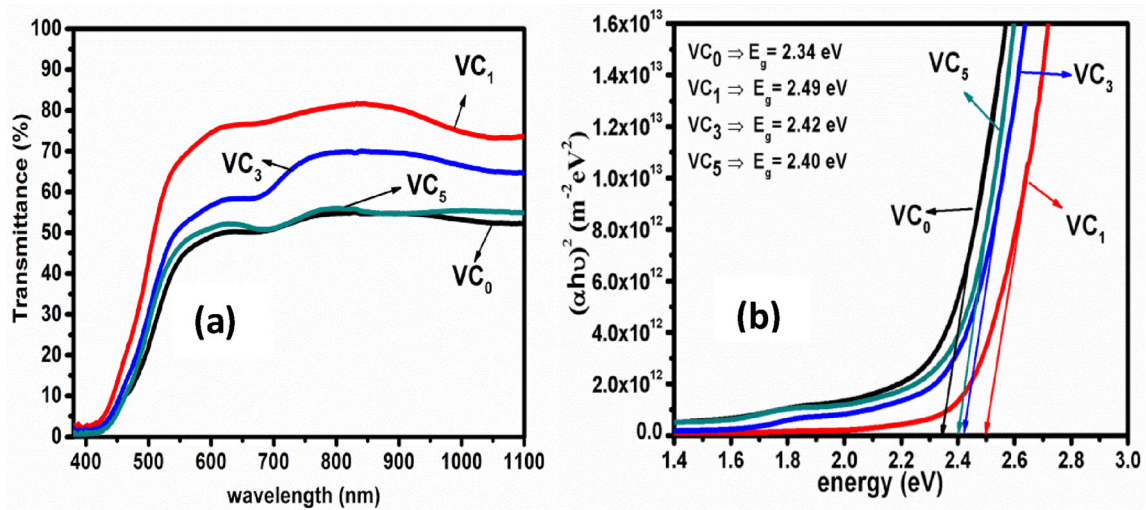


Fig. 3 a Optical transmittance of the films VC₀, VC₁, VC₃ and VC₅, and b Direct optical bandgap of the films VC₀, VC₁, VC₃ and VC₅ (Color figure online)

Table 2 Optical and electrical parameters of the films VC₀, VC₁, VC₃ and VC₅

Film	AVT (%) (500–800 nm)	$T_{max.}\%$ (λ) (nm)	E_g (eV)	Carrier concentration (cm^{-3})	Mobility (cm^2 $\text{V}^{-1} \text{s}^{-1}$)	Conductivity ($\Omega^{-1} \text{cm}^{-1}$)
VC ₀	48	55.0 (830)	2.34	3.17×10^{19}	25.9	1.3×10^2
VC ₁	74	81.7 (844)	2.49	4.06×10^{19}	38.2	2.5×10^2
VC ₃	58	70.0 (840)	2.42	2.81×10^{19}	34.3	1.6×10^2
VC ₅	50	56.0 (798)	2.40	2.77×10^{19}	33.5	1.4×10^2

(film VC₁) shows effective variation in the electrical transport properties. This may be due to the formation of hollow microspheres by the nanorods structures which allow the electrons to flow freely.

3.5 Electrochemical analysis

3.5.1 Cyclic voltammetry

Cyclic voltammetry (CV) measurements were performed to investigate the anodic and cathodic behavior of electrochromic property of V₂O₅ and V₂O₅/MWCNT composite films. Figure 4 shows the CVs of films VC₀, VC₁, VC₃ and VC₅ measured at 5 mV s⁻¹ sweep rate in a potential range from -0.5 to 0.95 V (vs Ag/AgCl). When the potential is swept towards -0.55 V, the intercalation of Li⁺ and electrons into V₂O₅ matrix forms lithium vanadate bronze (Li_xV₂O₅) and shows color changes from yellow to green to blue. Further when the potential is reversed Li⁺ and electrons deintercalate at which

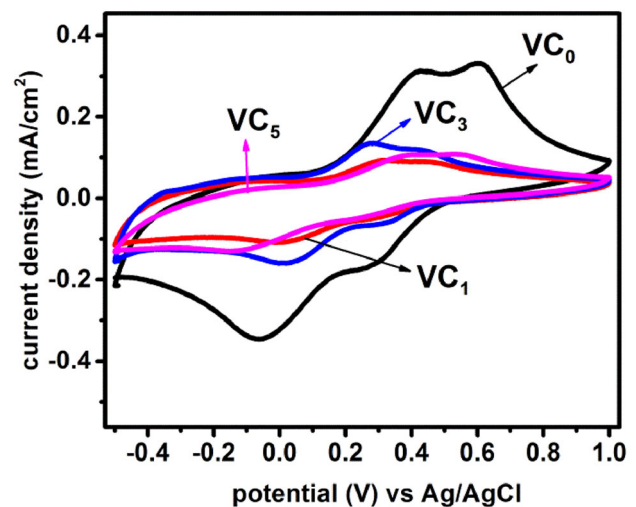


Fig. 4 CVs of the films VC₀, VC₁, VC₃ and VC₅ at a scan rate of 5 mV s⁻¹ (Color figure online)

Li_xV₂O₅ is oxidized to original state of V₂O₅ and changes the color from blue to green to yellow. The Li⁺ intercalation and deintercalation and the redox

Table 3 Diffusion coefficients calculated for the films VC₀, VC₁, VC₃ and VC₅

Film	Diffusion coefficient cm ² s ⁻¹ (× 10 ⁻⁹)			
	Intercalation		Deintercalation	
	Anodic 1st peak	Anodic 2nd peak	Cathodic 1st peak	Cathodic 2nd peak
VC ₀	26.8	30	7.1	32.8
VC ₁	5.0	3.8	1.0	7.0
VC ₃	2.4	2.2	0.6	3.2
VC ₅	3.0	3.1	0.7	4.5

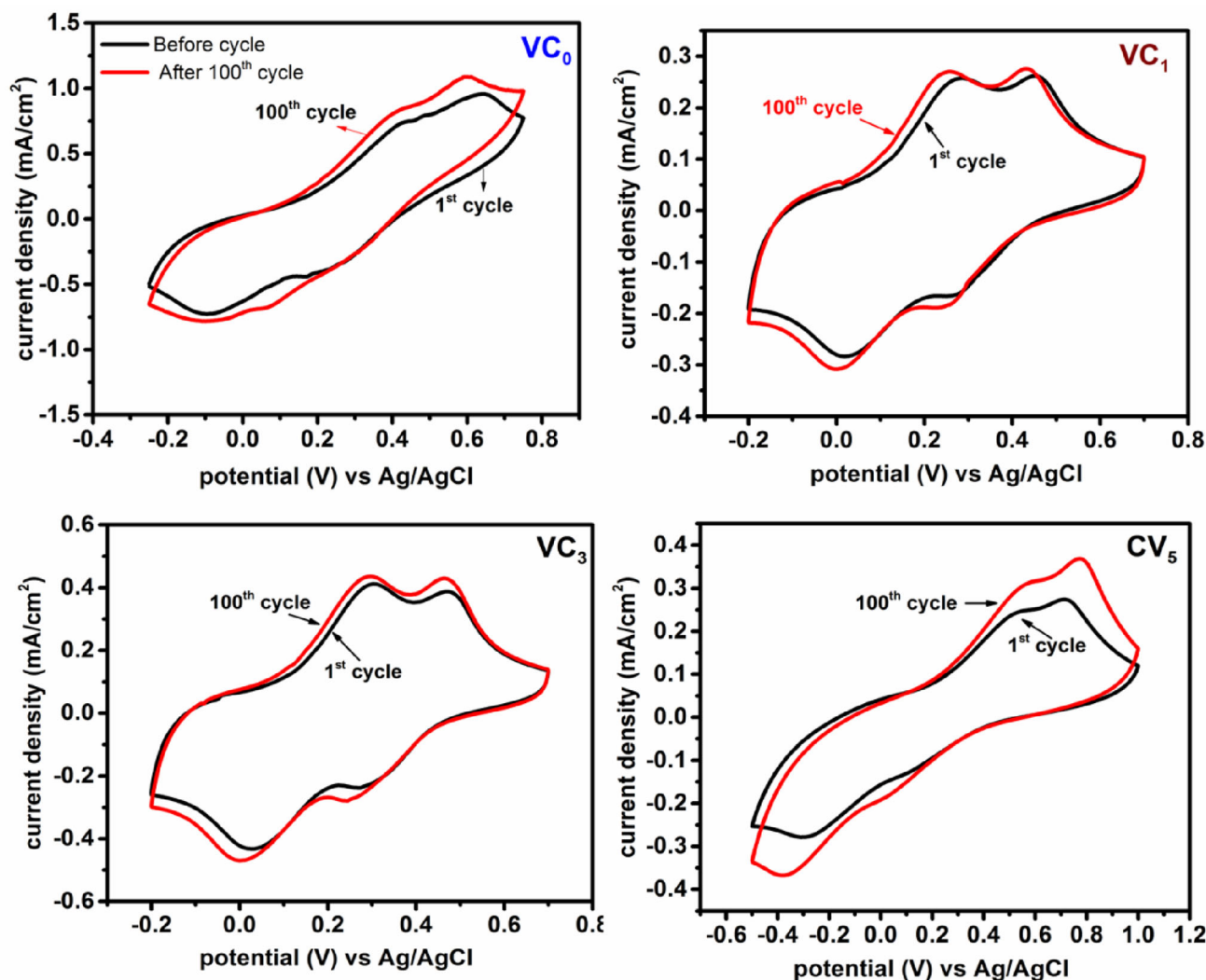


Fig. 5 CVs cyclic stability of the films VC₀, VC₁, VC₃ and VC₅ at scan rate of 10 mV s⁻¹ (Color figure online)

reaction between V⁴⁺ and V⁵⁺ is given by the equation $V_2O_5 + xLi^+ + xe^- \leftrightarrow Li_xV_2O_5$ [36]. Figure 4 reveals that the anodic and cathodic peak potential is shifted towards more negative and more positive values respectively in the films VC₁ and VC₃. The film VC₅ shows increase in anodic peak potential and

decrease in the cathodic peak potential due to saturated chemical interactions between MWCNTs and V₂O₅.

The diffusion coefficient of Li⁺ was obtained using well known Randles–Servick’s equation [37]

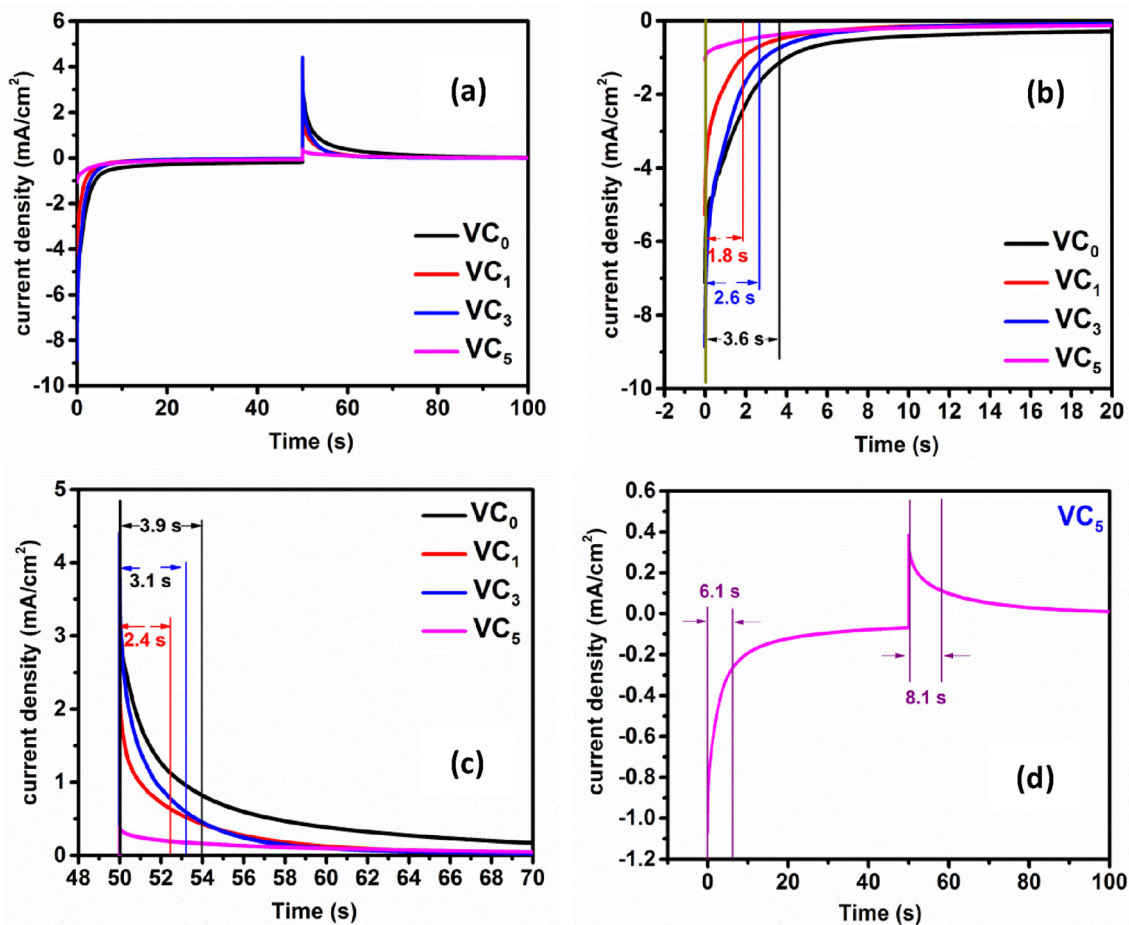


Fig. 6 **a** Switching time for the films VC₀, VC₁, VC₃ and VC₅, **b** response time for the films VC₀, VC₁, VC₃ and VC₅ to get in colored state, **c** response time for the films VC₀, VC₁, VC₃ and

VC₅ to get in bleached state, and **d** response time for the films VC₅ (Color figure online)

$$D = i_p / \left(2.69 \times 10^5 \times n^{3/2} \times A \times C_0 \times v^{1/2} \right),$$

where i_p is the peak current density, n is the number of electrons involved in the redox process, A is the area of the working electrode, C_0 is the concentration of Li⁺ and v is the scan rate. The calculated values of diffusion coefficient for Li⁺ in V₂O₅ and V₂O₅/MWCNT composite films are listed in Table 3.

The electrochemical stability of the films determined by cyclic voltammetry measurements with potential varying between -0.2 and 0.75 V (for films VC₀, VC₁ and VC₃) and between -0.5 and 1 V (for film VC₅) at a scan rate of 10 mV s^{-1} from 1 to 100 cycles is shown in Fig. 5. The current density increases from 1st cycle to 100th cycle for the films VC₀ and VC₅. The films VC₁ and VC₃ show slight increase in current density without significant changes in the shape of the CVs. The film VC₅ shows less

stability as has been observed in the film VC₀; this may be due to the formation of microplates like structure which hinders the Li⁺ ions intercalation/deintercalation owing to the capture of Li⁺ ions inside the compact microplate structures as compared to hollow microsphere structures formed in the films VC₁ and VC₃.

3.5.2 Chronoamperometry

The switching kinetics of the films VC₀, VC₁, VC₂ and VC₃ are important especially for the practical application. Figure 6a shows the switching time for the films VC₀, VC₁, VC₃ and VC₅ and the values are compared with the literature values in Table 4. Figure 6b displays the response time observed in the films VC₀, VC₁ and VC₃ corresponding to the change from bleached state to colored states whereas Fig. 6c

Table 4 Comparison of response time for the films VC₀, VC₁, VC₃ and VC₅ obtained initially and after 100 cycles of CVs with the reported values

Samples	Before 100 cycle of CVs		After 100 cycle of CVs		Refs.
	Coloration	Response time (s)		Bleaching	
		Bleaching	Coloration		
VC ₀	3.6	3.9	4.9	5.6	PW
VC₁	1.8	2.4	2.2	3.0	PW
VC ₃	2.6	3.1	3.3	4.6	PW
VC ₅	6.1	8.1	9.0	11.5	PW
V ₂ O ₅	19.5	20.5	–	–	[13]
2 at.% Mg doped V ₂ O ₅	17	15	–	–	
15 at.% Mg doped V ₂ O ₅	10	4	–	–	
V ₂ O ₅	6.3	11.8	–	–	[17]
V ₂ O ₅ /rGO	4.4	7.3	–	–	
V ₂ O ₅ (200 nm thickness)	21.4	10.8	–	–	[36]
V ₂ O ₅ (400 nm thickness)	5.5	5.7	–	–	
Dense V ₂ O ₅	13.1	13.5	–	–	[37]
V ₂ O ₅ (210 nm pore size)	1.7	3.2	–	–	
V ₂ O ₅ (340 nm pore size)	2.2	5.7	–	–	
V ₂ O ₅ (840 nm pore size)	3.0	3.5	–	–	
V ₂ O ₅	23	20	20	27	[38]
V ₂ O ₅ nanowire	6	5	–	–	[39]
Dense V ₂ O ₅	9.8	11.5	–	–	[40]
3D ordered macroporous V ₂ O ₅	1.5	2.1	–	–	
V ₂ O ₅	2	4	–	–	[41]

reveals the response time for the films corresponding to change from colored state to bleaching state. The response time for the film VC₅ is shown in Fig. 6d. The film VC₁ (1 wt% of MWCNT) exhibits fastest switching time of 1.8 s for the change from colored to bleached state and 2.4 s switching time for the change from bleached state to colored state. Switching time observed for the film VC₁ is relatively faster when compared with the switching times of other films in the present work (VC₀, VC₃ and VC₅) and that of the films reported in the literature [13, 17, 38–43]. These values are compared in Table 4. The switching times calculated after 100 cycles in the CVs measurements for all the films are presented in Fig. 7a–d and the details are given in Table 4. After 100 cycles of CVs, the coloration and bleaching times for the film VC₁ show fastest response when compared to that of the other films. Because of the higher trap of Li⁺ in the V₂O₅ matrix, the reaction time for all deposited films after 100 cycles is elevated.

3.5.3 Chronocoulometry

Chronocoulometry measurements of the films VC₀, VC₁, VC₃ and VC₅ were carried out before and after 100 cycles of CV at the voltage swept from – 0.5 to 1 V with steps of 30 s to calculate the intercalation and deintercalation of Li⁺. The results are presented in Fig. 8a, b. In the forward condition, the films are colored because of the intercalation of charges due to diffusion process and the reduction of V⁵⁺ to V⁴⁺. Whereas in the reverse condition the films are bleached because of deintercalating the Li⁺ due to applying positive potential which changes the oxidation states of vanadium from V⁴⁺ to V⁵⁺. The electrochromic reversibility of films can be calculated using the ratio of the deintercalated charge (Q_{di}) to the intercalated charge (Q_i) (for coloration/bleaching after 30 s) using the following relation [44]

$$\text{Reversibility} = Q_{di}/Q_i.$$

The calculated percentage of electrochromic reversibility for the coated films before and after 100 cycles is listed in Table 5. The electrochromic reversibility obtained before performing 100 cycles

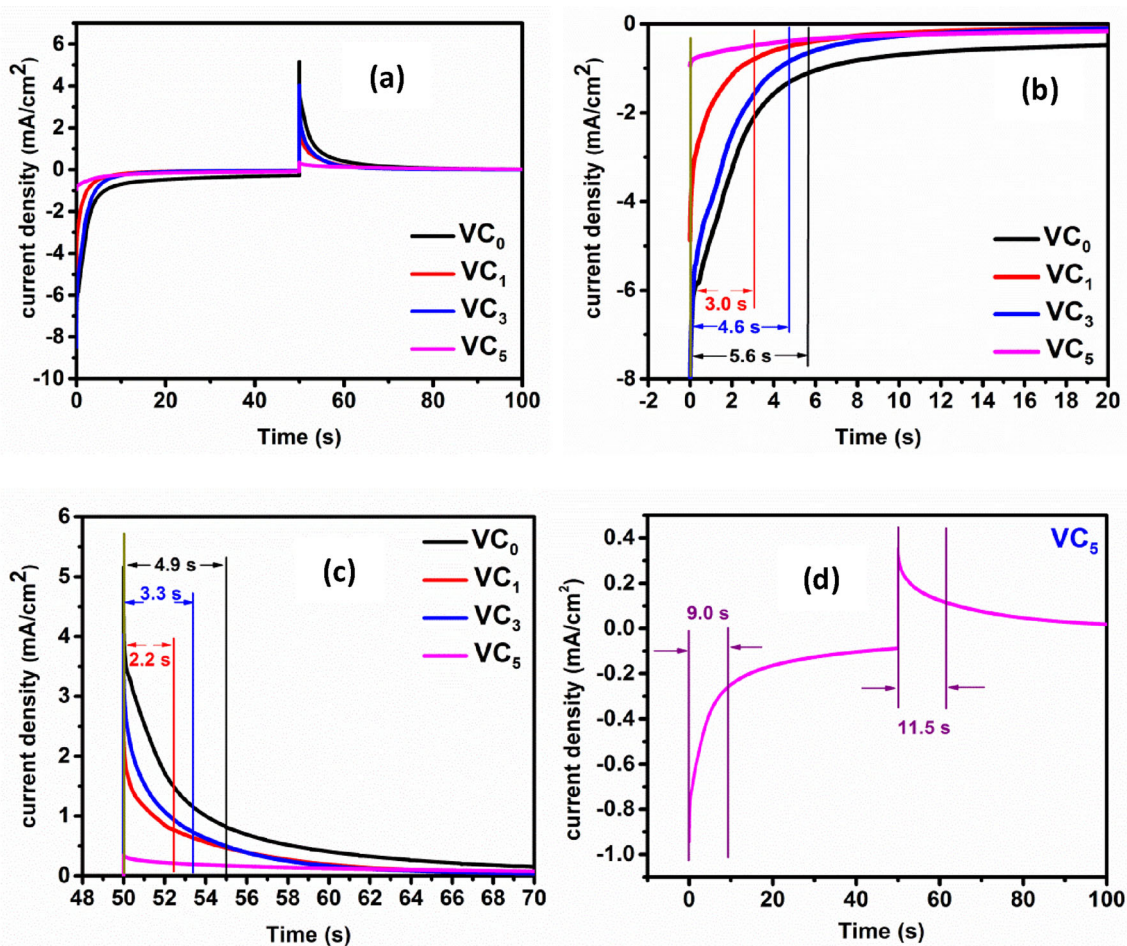


Fig. 7 **a** After 100 cycles of CVs, switching time calculated for the films VC₀, VC₁, VC₃ and VC₅, **b** after 100 cycles of CVs, response time calculated for the films VC₀, VC₁, VC₃ and VC₅ to get in colored state, **c** after 100 cycles of CVs, response time for

the films VC₀, VC₁, VC₃ and VC₅ to get in bleached state, and **d** after 100 cycles of CVs, response time for the films VC₅ (Color figure online)

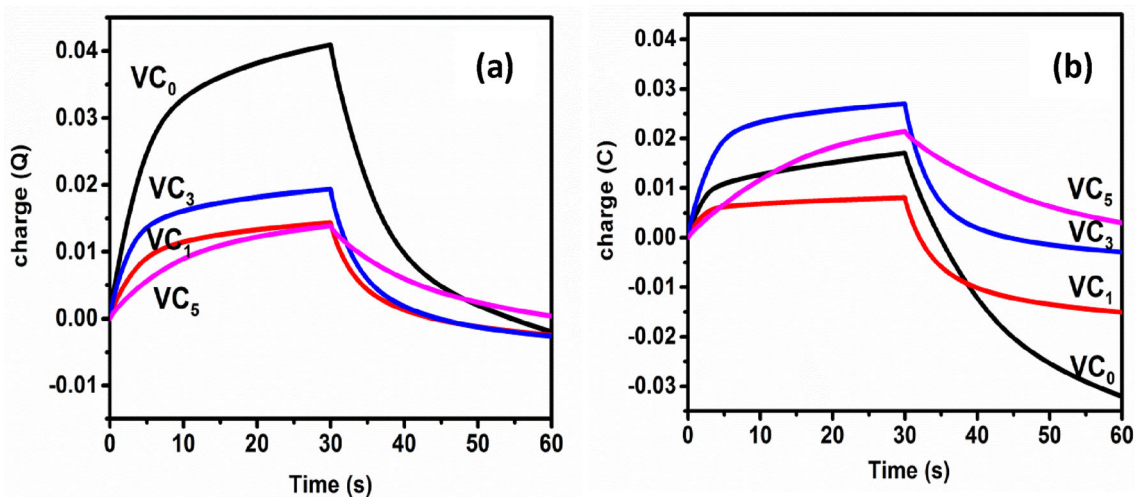
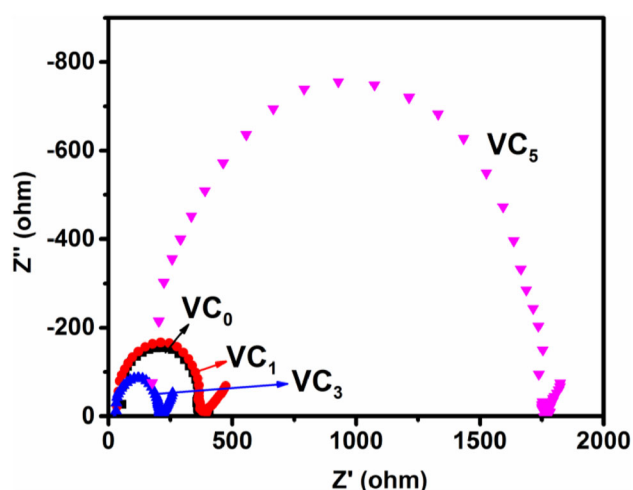


Fig. 8 **a** Chronoamperometry response of the films VC₀, VC₁, VC₃ and VC₅, and **b** after 100 cycles of CVs, chronoamperometry response of the films VC₀, VC₁, VC₃ and VC₅ (Color figure online)

Table 5 Reversibility for the films VC₀, VC₁, VC₃ and VC₅ obtained initially and after 100 cycles of CVs

Before 100 cycle of CVs				After 100 cycle of CVs				
Film	Q_i	Q_{di}	Residual charge (Q_r)	Reversibility (%)	Q_i	Q_{di}	Residual charge (Q_r)	Reversibility (%)
VC ₀	0.0400	0.0383	0.0017	95.8	0.0167	-0.0153	0.032	91
VC ₁	0.0140	0.0115	0.0025	82.1	0.0078	-0.0073	0.0150	92
VC ₃	0.0143	0.0118	0.0025	82.5	0.0268	0.0237	0.0031	88
VC ₅	0.0137	0.0133	0.0003	97.2	0.0213	0.0183	0.0030	86

**Fig. 9** Nyquist plots of films VC₀, VC₁, VC₃ and VC₅ (Color figure online)

for the films VC₀ and VC₅ shows excellent reversibility of about 95.8% and 97.2% respectively due to good crystallinity as observed from XRD results (Fig. 1a) and dense microspheres morphology of the films. The films VC₁ and VC₃ respectively show about 82.1% and 82.5% electrochromic reversibility due to relatively less crystalline nature and less number of active microspheres. After 100 cycles of CVs, the estimated electrochromic reversibility decreases from 95.8 to 91% for the film VC₀ whereas for film VC₅ it decreases from 97.2 to 86% which indicates that some of the Li⁺ are trapped into microspheres during the diffusion process. Further the films VC₁ and VC₃ show relatively enhanced electrochromic reversibility from 82.1 to 92% and from 82.5 to 88% respectively due to interaction of MWCNT with V₂O₅.

3.5.4 Impedance measurements

The charge transfer process in the deposited films is investigated by the electrochemical impedance spectroscopy (Fig. 9). Nyquist plot of the films shows a semicircle and an inclined line respectively in the high frequency region and in low frequency region. The semicircle represents the migration of Li⁺ between the electrode and electrolyte interface whereas straight line indicates the Li⁺ diffusion into the bulk V₂O₅ material [45]. The free diffusion of the Li⁺ from an electrolyte as well as the electrons from the working electrode into the electrochromic layers results in the linear impedance spectrum that indicates the process of diffusion of Li⁺ and electrons into and out of the working electrode, i.e. V₂O₅ films [46]. The steeper slopes observed from low frequency tail for VC₀, VC₁, and VC₃ films represent higher Li⁺ conductivity in the electrode materials i.e., low value of charge transfer resistance indicates the presence of highly conductive ion migration during the intercalation/deintercalation process when compared to that of the film VC₅. The films VC₀, VC₁ and VC₃ exhibit relatively faster switching time when compared to that of film VC₅.

4 Conclusions

The V₂O₅/MWCNT composites films were successfully deposited by the hydrothermal technique on the FTO glass substrates. The peaks shift observed in Raman and FTIR analyses is due to the effect of MWCNT in V₂O₅/MWCNT composites films. The numbers of microspheres formed on the surface of the film V₂O₅/MWCNT (1 wt% MWCNT) is reduced and modified due to addition of 1 wt.% and 3 wt.% of MWCNT in the synthesis process. Enhanced transmission is observed for V₂O₅/MWCNT (1 wt.%)

composite film (VC₁) due to formation of hollow microspheres structures consisting nanorods and a slight increase in the bandgap value when compare with that of VC₀. The switching kinetics of the film VC₁ shows fastest coloration and bleaching time of 1.8 s and 2.8 s respectively due to increase in the conductivity and mobility of the film. The films VC₁ and VC₃ show excellent electrochromic reversibility of 92% and 88% respectively after 100 cycles in CV measurements; thus the improved stability of the films VC₁ and VC₃ is due to formation of hollow microsphere containing nanorods. The fastest switching kinetics and high reversibility (after 100 cycles) observed in the film VC₁ represent its suitability for electrochromic device application.

Acknowledgements

One of the authors (M.M.M) thanks SRM Institute of Science and Technology, Kattankulathur, for the award of SRM University Fellowship to carry out the research work. The authors thank Prof. D. John Thiruvadigal, Dean of Sciences and Dr. A. Karthigeyan, Head, Department of Physics and Nanotechnology, SRM Institute of Science and Technology for extending the facilities available in the department. The authors also thank DST – SERB – (YSS/2015/000651) for extending the facility of electrochemical workstation. The authors also thank CeNSE, IISc under INUP at IISc which have been sponsored by DeitY, MCIT, Government of India to carry out Raman studies and SEM analysis. The authors thank Dr. B. Neppolian, Professor and Dean Research, Research Institute, SRM Institute of Science and Technology, Kattankulathur for extending UV–Vis–IR Spectrophotometer facility.

Author contributions

MMM: Conceptualization, Methodology, Formal analysis, Writing- Original draft preparation SM: Conceptualization, formal analysis, Investigation, Writing—Review & Editing KR: Validation, Formal analysis, Writing—Review & Editing, VG: Resources, Writing—Review & Editing, RR: Resources, Writing—Review & Editing KS: Resources, Writing—Review & Editing.

Funding

The authors have no relevant financial or non-financial interests to disclose.

Data availability

The raw data are available at the corresponding author and can be presented for reasonable requests.

Declarations

Competing interests The authors declare that they have no competing interests.

References

1. G. Cai, J. Wang, P. See Lee, *Acc. Chem. Res.* **49**, 1469 (2016)
2. P. Jittiarporn, S. Badilescu, M.N. Al Sawafta, L. Sikong, T. Vo-Van, *J. Sci. Adv. Mater. Devices* **2**, 286 (2017)
3. A. Jin, W. Chen, Q. Zhu, Z. Jian, *Electrochim. Acta.* **55**, 6408 (2010)
4. H. Khmissi, S.A. Mahmoud, A.A. Akl, *Optik* **227**, 165979 (2021)
5. V. Balasubramani, J. Chandrasekaran, V. Manikandan, R. Marnadu, P. Vivek, P. Balrajuc, *Inorg. Chem. Commun.* **119**, 108072 (2020)
6. C. Xiong, A.E. Aliev, B. Gnade, K.J. Balkus Jr., *ACS Nano* **2**, 293 (2008)
7. M. Panagopoulou, D. Vernardou, E. Koudoumas, D. Tsoukalas, Y.S. Raptis, *Electrochim. Acta* **321**, 134743 (2019)
8. I. Mjejri, L.M. Mancieru, M. Gaudon, A. Rougier, F. Sediri, *Solid State Ion.* **292**, 8 (2016)
9. X. Ren, Y. Zhai, L. Zhu, Y. He, A. Li, C. Guo, L. Xu, *ACS Appl. Mater. Interfaces* **8**, 17205 (2016)
10. L. Chen, X. Gu, X. Jiang, N. Wang, J. Yue, H. Xu, J. Yang, Y. Qian, *J. Power Sources* **272**, 991 (2014)
11. J.H. Yao, Z.L. Yin, Z.G. Zou, Y.W. Li, *RSC Adv.* **7**, 32327 (2017)
12. G.P. Pandey, T. Liu, J. Emery Brown, Y. Yang, Y. Li, X. Susan Sun, Y. Fang, J. Li, *ACS Appl. Mater. Interfaces* **8**, 9200 (2016)
13. M. Panagopoulou, D. Vernardou, E. Koudoumas, N. Katsarakis, D. Tsoukalas, Y.S. Raptis, *J. Phys. Chem. C* **121**, 70 (2017)
14. Y. Wei, J. Zhou, J. Zheng, C. Xu, *Electrochim. Acta* **166**, 277 (2015)
15. S.R. Li, S.Y. Ge, Y. Qiao, Y.M. Chen, X.Y. Feng, J.F. Zhu, C.H. Chen, *Electrochim. Acta* **64**, 81 (2012)

16. X. Zhang, H. Sun, Z. Li, J. Xu, S. Jiang, Q. Zhu, A. Jin, G.S. Zakharova, *J. Electrochem. Soc.* **160**, H587 (2013)
17. M. Zhi, W. Huang, Q. Shi, B. Peng, K. Ran, *J. Electrochem. Soc.* **163**, H891 (2016)
18. X.M. Liu, Z.D. Huang, S. Oh, P.C. Ma, P.C.H. Chan, G.K. Vedam, K. Kang, J.K. Kim, *J. Power Sources* **195**, 4290 (2010)
19. M. Qin, J. Liu, S. Liang, Q. Zhang, X. Li, Y. Liu, M. Lin, *J. Solid State Electrochem.* **18**, 2841 (2014)
20. T. Adschiri, Y. Hakuta, K. Arai, *Ind. Eng. Chem. Res.* **39**, 4901 (2000)
21. L. Hongjiang, G. Yanfeng, Z. Jiadong, L. Xinling, C. Zhang, C. Chuanxiang, L. Hongjie, K. Minoru, *J. Solid State Chem.* **214**, 79 (2014)
22. A. Fallah-Shojaei, K. Tabatabaieian, F. Shirinia, S. Zoha Hejazia, *RSC Adv.* **4**, 9509 (2014)
23. P. Scherrer, *Nachr. Ges. Wiss. Göttingen* **26**, 98 (1918)
24. J.I. Langford, A.J.C. Wilson, *J. Appl. Cryst.* **11**, 102 (1978)
25. W.C. Fang, *J. Phys. Chem. C* **112**, 11552 (2008)
26. T. Kim, H. Kim, T.S. You, J. Kim, *J. Alloys Compd.* **727**, 522 (2017)
27. A. Bilal, G.R. Khan, K. Asokan, *RSC Adv.* **5**, 52602 (2015)
28. H. Zhao, L. Pan, S. Xing, J. Luo, J. Xu, *J. Power Sources* **222**, 21 (2013)
29. J. Shin, H. Jung, Y. Kim, J. Kim, *J. Alloys Compd.* **589**, 322 (2014)
30. C. Xiong, E.A. Ali, G. Bruce, J.B. Kenneth, *ACS Nano* **2**, 293 (2008)
31. W. Chen, L. Qiang Mai, J. Feng Peng, Q. Xu, Q. Yao Zhu, *J. Mater. Sci.* **39**, 2625 (2004)
32. Q. He, X. Xiangdong, W. Meng, S. Minghui, J. Yadong, Y. Jie, A. Tianhong, *Phys. Chem. Chem. Phys.* **18**, 1422 (2016)
33. J.I. Pankove, *Optical Processes in Semiconductors* (Prentice-Hall Inc., Englewood Cliffs, 1971), p.36
34. E. Burstein, *Phys. Rev.* **93**, 632 (1954)
35. T.S. Moss, *Proc. Phys. Soc. Sect. B* **67**, 775 (1954)
36. B. Klaus, T. Gambke, G. Sparschuh, in: R.E. Hummel, K.H. Guenther (Eds.), *Optically Active Thin Film Coatings, Handbook of Optical Properties: Thin Films for Optical Coatings*, (CRC Press, Boca Raton, 1995), p. 123
37. C.G. Granqvist, *Handbook of Inorganic Electrochromic Materials* (Elsevier, Amsterdam, 1995), pp.1–3
38. E. Eren, G. Yurdabak Karaca, C. Alver, A. Uygun Oksuz, *Eur. Polym. J.* **84**, 345 (2016)
39. Z. Tong, J. Hao, K. Zhang, J. Zhao, B.L. Suc, Y. Li, *J. Mater. Chem. C* **2**, 3651 (2014)
40. U. Tritschler, F. Beck, H. Schlaad, H. Cölfen, *J. Mater. Chem. C* **3**, 950 (2015)
41. K. Che Cheng, F.R. Chen, J. Jung Kai, *Sol. Energy Mater. Sol. Cells* **90**, 1156 (2006)
42. Z. Tong, H. Yang, L. Na, H. Qu, X. Zhang, J. Zhao, Y. Li, *J. Mater. Chem. C* **3**, 3159 (2015)
43. W. He, Y. Liu, Z. Wana, C. Jia, *RSC Adv.* **6**, 68997 (2016)
44. S. Poongodi, P. Suresh Kumar, Y. Masuda, D. Mangalaraj, N. Ponpandian, C. Viswanathana, S. Ramakrishna, *RSC Adv.* **5**, 96416 (2015)
45. W. Man, H. Lu, L. Ju, F. Zheng, M. Zhang, M. Guo, *RSC Adv.* **5**, 106182 (2015)
46. K.S. Usha, R. Sivakumar, C. Sanjeeviraja, S. Vasant, V. Ganesan, T.Y. Wange, *RSC Adv.* **6**, 79668 (2016)

Publisher's Note Springer Nature remains neutral with regard to jurisdictional claims in published maps and institutional affiliations.

Springer Nature or its licensor holds exclusive rights to this article under a publishing agreement with the author(s) or other rightsholder(s); author self-archiving of the accepted manuscript version of this article is solely governed by the terms of such publishing agreement and applicable law.